Chemical Science

ROYAL SOCIETY OF CHEMISTRY

EDGE ARTICLE

View Article Online
View Journal

Cite this: DOI: 10.1039/d5sc05330g

All publication charges for this article have been paid for by the Royal Society of Chemistry

Alkaline electrocatalytic water oxidation by Fe–Ni nanostructures on porous turbostratic carbon with tailorable metal–metal active sites

Dipankar Saha, [a] Chaoyun Tang,[b] Javed Khan,[b] Pulkit Jain,[b] Cheng-Jie Yang,[c] Chung-Li Dong, [c] Richard F. Webster, [d] Chi-Liang Chen, [e] Zhu Chen,[b] Peng Bai, [b] Richard M. Tilley, [df] Nianqiang Wu *[b] and James J. Watkins *[a]

Metal ensembles on carbon supports enhance electrocatalysis by requiring close metal–metal proximity, but controlling their clustering remains difficult with current synthesis methods. This study presents a one-step high-throughput synthesis using a bottlebrush block copolymer (BBCP) template, dopamine, and metal precursors (Fe and Ni salts), which can generate high metal loadings (4 at%) of bimetallic Fe–Ni nanostructures with a reduced metallic oxidation state. The BBCP template and polymerized dopamine create a porous carbon matrix upon carbonization. Rapid photothermal pyrolysis, a photonic curing technique, carbonizes samples in seconds, creating uniform Fe–Ni active sites with reduced time and low cost. The short time scales of carbonization and metal precursor reduction favor high metal dispersion, small cluster formation, and the reduced metal oxidation state, all crucial for catalyst performance. In oxygen evolution reaction (OER) testing, the Fe–Ni/N–C catalyst showed a 130 mV overpotential at 10 mA cm^{-2} and a Tafel slope of 40 mV per dec in 1 M KOH. Tailorable Ni–Fe active sites enable high activity and stability, achieving 100 mA cm^{-2} at 1.75 V in 1 M KOH at 80 °C with an alkaline membrane electrode assembly (MEA). The unique synthesis approach enables rapid, large-scale production of high-performance electrocatalysts with tunable metal–metal sites, advancing sustainable fuel generation.

Received 17th July 2025
Accepted 20th December 2025

DOI: 10.1039/d5sc05330g

rsc.li/chemical-science

Introduction

Isolated single-atom catalysts (SACs) and nanoclusters offer superior atom efficiency and unique electronic properties, especially with noble metals.[1,2] Changes in metal size affect not just the domain size but also coordination, valence states, and geometric configuration, influencing reaction rates and selectivity. It has been reported that alloying with an inert metal can suppress hydrogenolysis while allowing dehydrogenation, introducing the concept of the ensemble requirement of the minimum number of metal atoms needed for efficient catalysis.[3] This concept was later extended to metal nanoparticles and clusters, focusing on the optimal metal atom count for performance. To enhance catalytic performance, isolated metal atoms are now integrated with carbon or oxides to form hybrid catalysts that provide (a) synergistic improvements in activity and selectivity by modulating electron structures and (b) increased active sites, enhancing efficiency in multi-step or parallel reactions. These hybrid systems help metal dispersion, control particle size and stabilize the atomic structure and reduce agglomeration.[4–7] Despite significant progress, the synthesis process remains complicated and often involves substantial trial and error, and the reaction mechanisms of these hybrid catalysts are not fully understood. For example, currently, the most common methods for preparing metal-based catalysts, including alloys and individual metals, involve using metal–organic precursors like metal–organic frameworks (MOFs) or metal-porphyrin complexes.[8,9] These are typically followed by high-temperature carbonization to embed metal atoms into a carbon matrix. However, the complexity, instability, low conductivity issues, and low yields of these synthesis processes hinder large-scale production.[10] Additionally, prolonged high temperatures (over 8 hours) can lead to surface reshaping and sintering of metal particles, reducing catalytic activity.[11,12] Since thermal annealing is commonly used for carbonization, controlling the annealing process while maintaining the internal structure is crucial for synthesizing metal nanostructured catalysts. Thus, there is a clear need for

[a]Conte Center for Polymer Research, Department of Polymer Science and Engineering, University of Massachusetts, Amherst, Massachusetts 01003, USA. E-mail: watkins@polysci.umass.edu
[b]Department of Chemical and Biomolecular Engineering, University of Massachusetts, Amherst, Massachusetts 01003, USA. E-mail: nianqiangwu@umass.edu
[c]Department of Physics, Tamkang University, Tamsui, 25137, Taiwan
[d]Mark Wainwright Analytical Centre, The University of New South Wales, Sydney, NSW 2052, Australia
[e]National Synchrotron Radiation Research Center, Hsinchu 30076, Taiwan
[f]School of Chemistry, The University of New South Wales, Sydney, NSW 2052, Australia

efficient synthesis methods that integrate ultrafine metal ensembles (single atoms, clusters, or nanoparticles) into hybrid catalysts, which are essential for dispersing ultrafine metal ensembles and preventing metal aggregation to create high-performance catalysts for industrial-scale applications.

Recently, we synthesized porous carbon structures doped with N and Fe, achieving isolated Fe atoms and clusters using a bottlebrush block copolymer (BBCP) with hematin porcine and melamine formaldehyde, followed by rapid thermal annealing (RTA) in minutes.[6] To further simply the synthesis process and to improve catalyst performance, a one-step synthesis method is preferred than a multi-step approach. Also, synthetic method should not only accommodate metal atoms but also promote the formation of an ordered graphitic structure in a metal–heteroatom–carbon arrangement. While our previous method produced a limited number of isolated metal atoms with relatively short carbonization times, there is potential to further reduce time without sacrificing the integrity of the material. This could increase the metal density, including a higher concentration of isolated metal atoms, which would enhance catalytic performance by providing more accessible active sites.

Here, we present a straightforward, one-step synthesis method that combines self-assembly with rapid photothermal pyrolysis to create a hybrid catalyst, as confirmed by Aberration-Corrected High-Angle Annular Dark-Field Scanning Transmission Electron Microscopy (AC HAADF-STEM). These catalysts are composed of primarily of bimetallic Fe–Ni nanoparticles, along with isolated metal atoms and clusters, all supported on a predominantly ordered graphitic carbon framework. This method significantly enhances metal atom density with high dispersion, achieving high contents of Fe and Ni in the hybrid catalyst. The Fe–Ni electrocatalyst demonstrates excellent stability in alkaline environments, low overpotentials, and outstanding performance in alkaline membrane electrode assembly (MEA) water-splitting devices, comparable to noble metal catalysts such as Pt/C and RuO_2. Further, *in situ* Raman spectroscopy and density functional theory (DFT) studies offer valuable insights into the ensemble requirements for Fe–Ni, providing insights into how the arrangement and interaction of metal atoms influence catalytic performance. These results highlight the synergistic effects of active sites in hybrid electrocatalysts, offering a pathway to design efficient and durable earth-abundant catalysts beyond single metal atoms for electrocatalysis.

Results and discussion

Synthesis of Fe–Ni nanostructures and impact of photothermal pyrolysis

In this study, we used amphiphilic PS-*b*-PEO BBCPs that self-assemble into spherical micelles in a water/ethanol mixture, which subsequently form a porous structure. Dopamine was used to generate an N- and O-doped ordered graphitic structure (turbostratic carbon) during polymerization, while iron (Fe) and nickel (Ni) were selected as the metal sites. Both metals are low-cost, abundant, and capable of forming hierarchical nanostructures on ordered carbon. Furthermore, Fe and Ni are ideal choices for earth-abundant catalytic support materials for oxygen evolution reaction (OER), as evidenced by their use in commercial stainless steels and nanofoams, which are among the most advanced electrode support materials.[13–15] A total metal loading of 10 wt% was chosen based on OER performance (discussed later), where we varied the Fe to Ni ratio to investigate the loading at which the OER activity begins to decline.

The Fe–Ni nanostructures on ordered carbon were prepared with a one-pot synthesis process (Fig. 1a). The Fe–Ni nanostructure features the coexistence of multiple metal size domains, ranging from isolated single atoms and small clusters to nanoscale particles. The intermediate product was characterized using a high-resolution transmission electron microscope (HRTEM) and HAADF-STEM, as detailed in Fig. 1c and e, and subsequently in Fig. 2. In the first two steps, polydopamine (PDA)/BBCP/Fe–Ni (total metal loading is 10 wt%) composite micelles were formed in a water/ethanol mixture, with the BBCP solution prepared in THF (Fig. 1b for photographic image). Dopamine molecules bind to the micelle surface through hydrogen bonding with the PEO block, while the hydrophobic polystyrene resides in the cores of the micelles.[16] The polystyrene cores serve as a sacrificial porogen and are later removed during the pyrolysis process, creating mesopores of controlled and tunable size in the structure.[17,18] Meanwhile, the heteroatoms (N and O) in dopamine interact with the metal salts, promoting their binding to the micelle surface.[19,20] Under alkaline conditions, the addition of ammonia triggers the self-polymerization of dopamine, leading to the formation of PDA/BBCP/Fe–Ni composite micelles. Key synthetic considerations in steps I and II include ensuring that all precursors are soluble in the chosen solvent mixture and controlling the cooperative assembly of the PS-*b*-PEO BBCP and dopamine to form spherical micelles. This was successfully achieved using a water–ethanol solvent mixture, allowing the BBCP to spontaneously template the spherical morphology.

The HRTEM image (Fig. 1c) reveals the micelle formation after 48 hours of reaction. The composite formed in step III (Fig. 1d for photographic image) was collected as a precipitate, but repeated washing with a water–ethanol mixture was necessary. The final Fe–Ni nanostructures on ordered graphitic mesoporous carbon in steps IV and V were achieved through rapid photothermal pyrolysis of the PDA/BBCP/Fe–Ni composite micelles, which were dried overnight under ambient conditions prior to pyrolysis. Next, the material underwent photothermal pyrolysis with a xenon flash lamp emission energy of 2.61 J cm^{-2} to rapidly heat materials to over 2000 °C (simulated temperature),[21] removing organic components, and transforming precursors through electronic, molecular, and phonon interactions. We have recently demonstrated the rapid and scalable formation of mesoporous silicas, mesoporous carbons, few-layer graphene, and ceramics using this approach.[22–25] Unlike conventional tube furnaces, which take over 8 hours to reach 800 °C, this method is much faster. Our fast process enabled the formation of new types of catalytically active sites compared to conventional annealing.

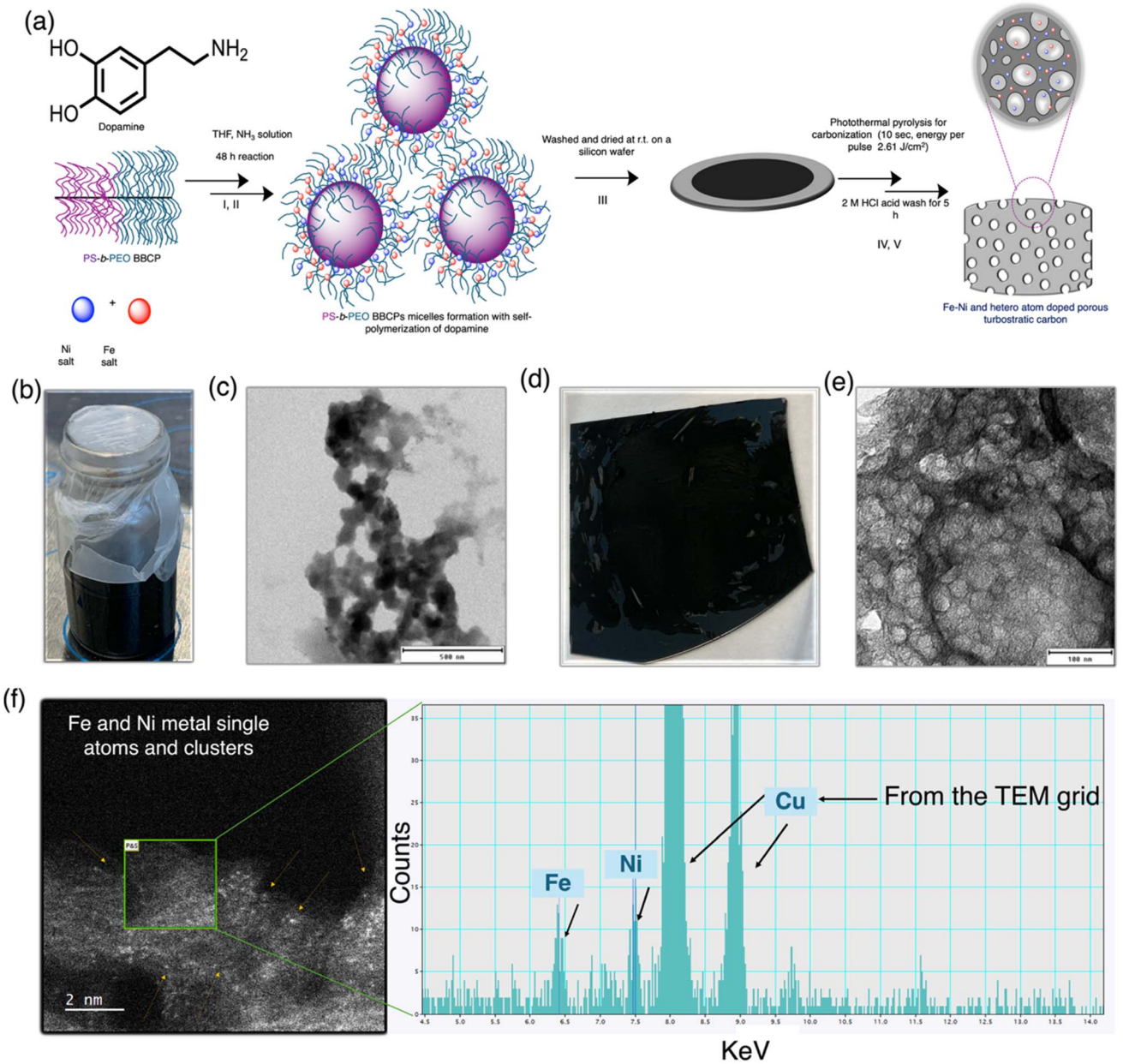

Fig. 1 Synthesis process of Fe–Ni nanostructures. (a) Schematic illustration of Fe–Ni structure formation (total metal loading is 10 wt%) at each synthetic step. (c and e) HRTEM and HAADF-STEM images of the nanostructures. (b and d) Photographic images of the synthesized material after steps I and III, (b) BBCP, dopamine, and metal salts are mixed to form the precursor in step I, (c) composite formation of BBCP/polydopamine/Fe, Ni metals with heteroatom as micelles in step II. The HRTEM image shows the micelle formation after 48 hours of reaction. The scale bar is 500 nm, (d) composite deposited for drying on a silicon wafer in step III, (e) the HRTEM (the scale bar is 100 nm) image reveals the material's porous structure of final heteroatom-doped hierarchical Fe–Ni obtained after photothermal pyrolysis, followed by a 5-hour acid wash in steps IV and V, (f) the green box in the HAADF-STEM image (scale bar is 2 nm) highlights the distribution of isolated Fe and Ni atoms, as well as small clusters, embedded within the graphitic matrix. The corresponding EDS intensity profile confirms the presence of Fe and Ni signals, while the Cu signals originate from the TEM grid.

The goal was to carbonize the BBCP/polydopamine/Fe–Ni composite into an ordered graphitic structure, maximizing the retention of heteroatoms and the reduced metallic state of Fe and Ni while preserving the integrity of the porous framework. It is essential to control the irradiation energy as too low an energy may prevent full carbonization, while too high an energy can damage the structure. This process resulted in the formation of mesopores within the carbon structure with hierarchical Fe–Ni metal. The HRTEM and HAADF-STEM images (Fig. 1e and f) reveal a well-defined porous structure with pore sizes of approximately 33 nm, as well as the presence of isolated Fe and Ni single atoms and small clusters. The EDS intensity profile further confirms the presence of Fe and Ni species. Corresponding images of the small nanoparticles are provided in Fig. 2. For comparison, individual Fe and Ni nanostructures

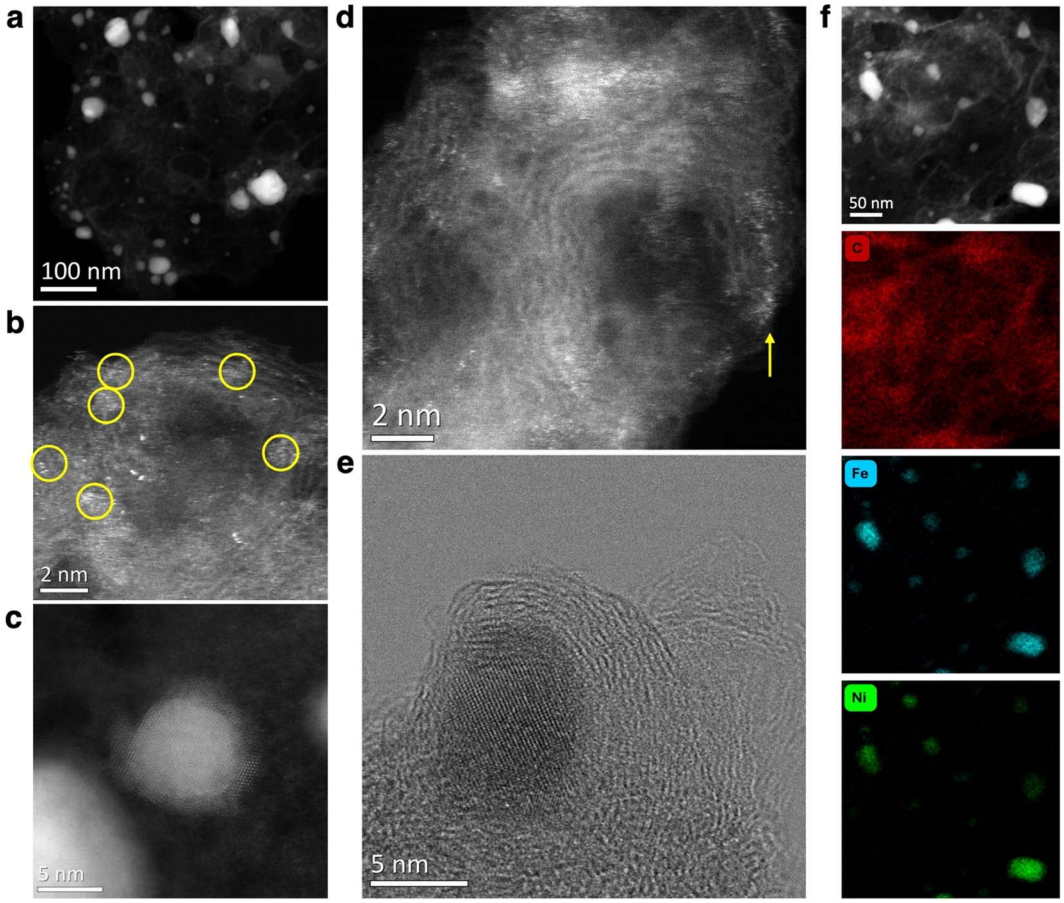

Fig. 2 Microscopic characterization of Fe–Ni nanostructures. (a) HAADF-STEM image of 10 wt% Fe–Ni nanoparticles; in (b) dense clusters of Fe–Ni atoms, highlighted with yellow circles, are seen alongside single atoms; (c) HAADF-STEM image of a Fe–Ni nanoparticle with an oxide shell. In (d), single atoms align with graphitic lattice planes, as indicated by the yellow arrow. (e) Left: bright field-STEM image of a Fe–Ni nanoparticle encapsulated by a graphitic shell (f) STEM-EDS map of Fe–Ni from a region with single atoms and nanoparticles showing the elemental distribution.

supported on porous carbon were also synthesized using the same procedure, each with a metal loading of 10 wt%.

Structural identification of Fe–Ni on porous turbostratic carbon

The as-synthesized hierarchical Fe–Ni metal nanostructure catalyst (10 wt% total metal loading) was examined by high-angle annular dark-field scanning transmission electron microscopy (HAADF-STEM) (Fig. 2). Inductively coupled plasma mass spectrometry analysis revealed that the metal content in the Fe–Ni nanostructure after carbonization was 4.7 wt% Fe and 4.9 wt% Ni. The analysis revealed nanoparticles predominantly in the 3–5 nm range, with an average size of 3.5 nm (Fig. 2a and S1). This average value was obtained from statistical analysis of over different particles across multiple HAADF-STEM and HRTEM images, which primarily captured the dominant nanoparticle population. Larger particles extending up to several tens of nanometers, occasionally observed in certain micrographs, constituted only a minor fraction of the overall population and were not significant in the statistical dataset used for Fig. S1. This observation was consistent with the STEM (Fig. 2c and e) and HRTEM (SI Fig. S4) images of the Fe–Ni structure. Furthermore, STEM analysis reveals that some particles possess a shell, likely corresponding to an oxide layer as indicated by the EDS mapping, while others are encapsulated within the carbon support (Fig. 2c, e and S2). These nanoparticles are uniformly dispersed on the carbon support with a high surface area of 237 $m^2 g^{-1}$, as determined by Brunauer–Emmett–Teller (BET) analysis, and exhibit mesoporosity (SI Fig. S3). The X-ray diffraction (XRD) pattern of the Fe–Ni metal nanostructure embedded in carbon (SI Fig. S4) shows distinct peaks that can be assigned to the intermetallic Fe–Ni phase. Specifically, the peaks at 43.3° and 51.3° were attributed to a mixture of face-centered cubic (fcc) and body-centered cubic (bcc) phases of the Fe–Ni alloy.[26]

No larger nanoparticles were found, suggesting they were removed during the 5-hour acid wash, which is insufficient for the removal of smaller nanoparticles in the turbostratic structure. High-magnification HAADF-STEM images further revealed the distribution of isolated Fe and Ni atoms (indicated by yellow circles and arrows in Fig. 2b and d, with additional HAADF images in Fig. S6). These isolated metal atoms are found near clusters, which were anchored to the turbostratic carbon

substrate alongside the nanoparticles. It was also observed that the isolated metal atoms preferentially aligned with the carbon substrate, often aligning with the graphitic lattice as arrowed in Fig. 2d. This suggests that the anchoring sites, likely provided by heteroatoms such as nitrogen and oxygen, are predominantly located in these regions, which attracted a higher concentration of metal atoms. This alignment was in favor to the stability of material, as the strong anchoring of metal atoms to these sites was expected to enhance their resistance to degradation, potentially leading to improved long-term stability during performance tests. The identification of these isolated spots was further confirmed by STEM combined with X-ray energy dispersive spectroscopy (EDS) elemental mapping (Fig. 2f and S7). The EDS spectrum of the Fe–Ni metal (Fig. S7) nanostructure clearly shows signals for both Fe and Ni. The EDS profile of the single atom within the yellow square reveals both Fe and Ni signals, indicating that this region corresponds to a Fe–Ni moiety embedded in the carbon support. The contrast between Fe and Ni spots in the STEM HAADF images is relatively subtle, as both elements have similar atomic numbers. This quantitative analysis confirmed that Fe and Ni were distributed across the entire region of the sample, with the single atoms likely being a mixture of both metals. Overall, the microscopic characterizations revealed the coexistence of abundant single Ni and Fe atoms alongside Fe–Ni nanoparticles within the hybrid material. The single atoms appear as isolated bright spots with sizes typically below 0.3 nm, exhibiting intensities consistent with individual metal atoms. Small clusters, consisting of aggregates of approximately 2–10 metal atoms, are observed as slightly larger and brighter features (0.3–1.5 nm) with well-defined boundaries but without visible crystalline lattice fringes. In contrast, nanoparticles are identified as larger entities exceeding 1.5 nm in size, generally ranging up to several nanometers in diameter.

To elucidate the local coordination environment and oxidation states of Fe and Ni in the Fe–Ni heterostructure (Fig. S8, for XPS survey), K-edge X-ray absorption spectroscopy (XAS) was carried out in comparison with the individual Ni–N–C and Fe–N–C reference materials (Fig. 3a, c and S9). The Ni K-edge X-ray absorption near-edge structure (XANES) spectrum of Ni–N–C exhibits (Fig. 3a) a relatively weak absorption intensity, with the edge position close to that of metallic Ni foil but distinctly shifted from NiO (nickel oxide) and NiPc (nickel phthalocyanine). Since the absorption edge position is positively correlated with oxidation state, the observed shift toward lower energy indicates that the Ni centers in Ni–N–C possess an average oxidation state below +2. This observation is further supported by the relatively low Ni 3d binding energy detected in the XPS spectrum (Fig. 3e). Similarly, the Fe K-edge XANES profile of Fe–N–C (Fig. 3c) displays a slight shift toward Fe foil and away from Fe_2O_3, FePc (iron phthalocyanine), and hematin porcine, suggesting that Fe species primarily exist in a mixed valence state between 0 and +3, with Fe^{2+} as the dominant form. The XPS analysis (Fig. 3e and f) further confirms these results: the Ni 2p spectrum of Ni–N–C reveals pronounced Ni^0 (852.7 eV, 70.9%) and Ni^{2+} (853.4 eV, 29.0%) components with negligible Ni^{3+} contribution, while the Fe 2p spectrum of Fe–N–C shows intense Fe^{2+} (707.2 eV, 65.6%) and Fe^0 (34.3%) signals (Fig. 3b). Collectively, these data indicate that Ni–N–C mainly consists of Ni^0 species, whereas Fe–N–C is dominated by Fe^{2+} sites, with minor contributions from Ni^{2+} and Fe^0. In the Fe–Ni heterostructure, both Ni and Fe K-edge XANES spectra exhibit distinct features relative to the single-metal systems (Fig. 3a and c). The Ni edge position remains near that of Ni foil but shows a small positive shift, suggesting the presence of Ni^0 species that are not bound through Ni–Ni metallic bonding. Meanwhile, the Fe K-edge indicates Fe primarily exists in the +2 oxidation state. High-resolution XPS analyses further validate these findings (Fig. 3e and f). The slight edge shifts of both Fe and Ni suggest that Fe–Ni heteroatomic interactions form intermetallic Fe–Ni bonds rather than isolated Fe–Fe or Ni–Ni networks.[27] Detailed analysis of the pre-edge region provides further insight into the local coordination geometry.[28] In the Ni K-edge XANES of Ni–N–C (Fig. 3a), a stronger pre-edge feature (8330–8340 eV) compared to NiPc arises from enhanced 1s → 3d quadrupole transitions, reflecting significant 3d-4p hybridization and local structural distortion.[29] The higher intensity ratio of features III to IV confirms asymmetric and defective Ni–N coordination environments, indicative of unsaturated Ni sites. Similarly, the Fe K-edge XANES of Fe–N–C displays (Fig. 3c)a single pre-edge peak, characteristic of off-planar Fe–N_4 coordination.[30] The peaks at 7132 and 7140 eV correspond to Fe–N_4 configurations with D_4h symmetry, where increased pre-edge intensity relative to FePc reveals off-centered Fe atoms and geometric distortion.[31] Comparable spectral trends are observed in the Fe–Ni/N–C heterostructure, where both Fe and Ni centers exhibit asymmetric, non-centrosymmetric coordination geometries.[32] Combined XANES and XPS analyses confirm that Fe–Ni/N–C contains Fe predominantly in the +2 oxidation state and Ni in the 0 oxidation state, with edge shifts and spectral features indicating Fe–Ni intermetallic coupling rather than Fe–Fe or Ni–Ni aggregation, consistent with the atomic-scale heterostructure design.

To further examine the coordination environment, Fourier-transform extended X-ray absorption fine structure (FT-EXAFS) analyses were performed on Ni–N–C, Fe–N–C, and Fe–Ni/N–C (Fig. 3b and d). All spectra exhibit main peaks between 1.3 and 1.5 Å, corresponding to the first coordination shell involving Ni–N/Fe–N or Ni–O/Fe–O bonds. Relative to NiPc and FePc, weaker peaks around 1.45 Å in the heterostructured samples indicate partial metal–oxygen coordination alongside metal–nitrogen bonding.[33] These results are consistent with high-resolution XPS analyses of the N 1s and O 1s regions (Fig. 3g and h), which reveal dominant graphitic nitrogen species with contributions from pyridinic and pyrrolic N, and oxygen peaks at 530.0 eV and 531.3 eV assigned to metal-oxide and metal-hydroxide bonds. Comparison with metallic and oxide standards in EXAFS also suggests the presence of weak metal–metal interactions in all samples, implying that not all Fe and Ni centers are fully isolated by nitrogen ligands. This too is supported by our XPS and HAADF-STEM observations. Notably, while the second-shell FT-EXAFS peaks of Fe–N–C and Ni–N–C align closely with their metallic references, those of Fe–Ni/N–C shift slightly to ~2.1 Å, indicating the formation of Fe–Ni

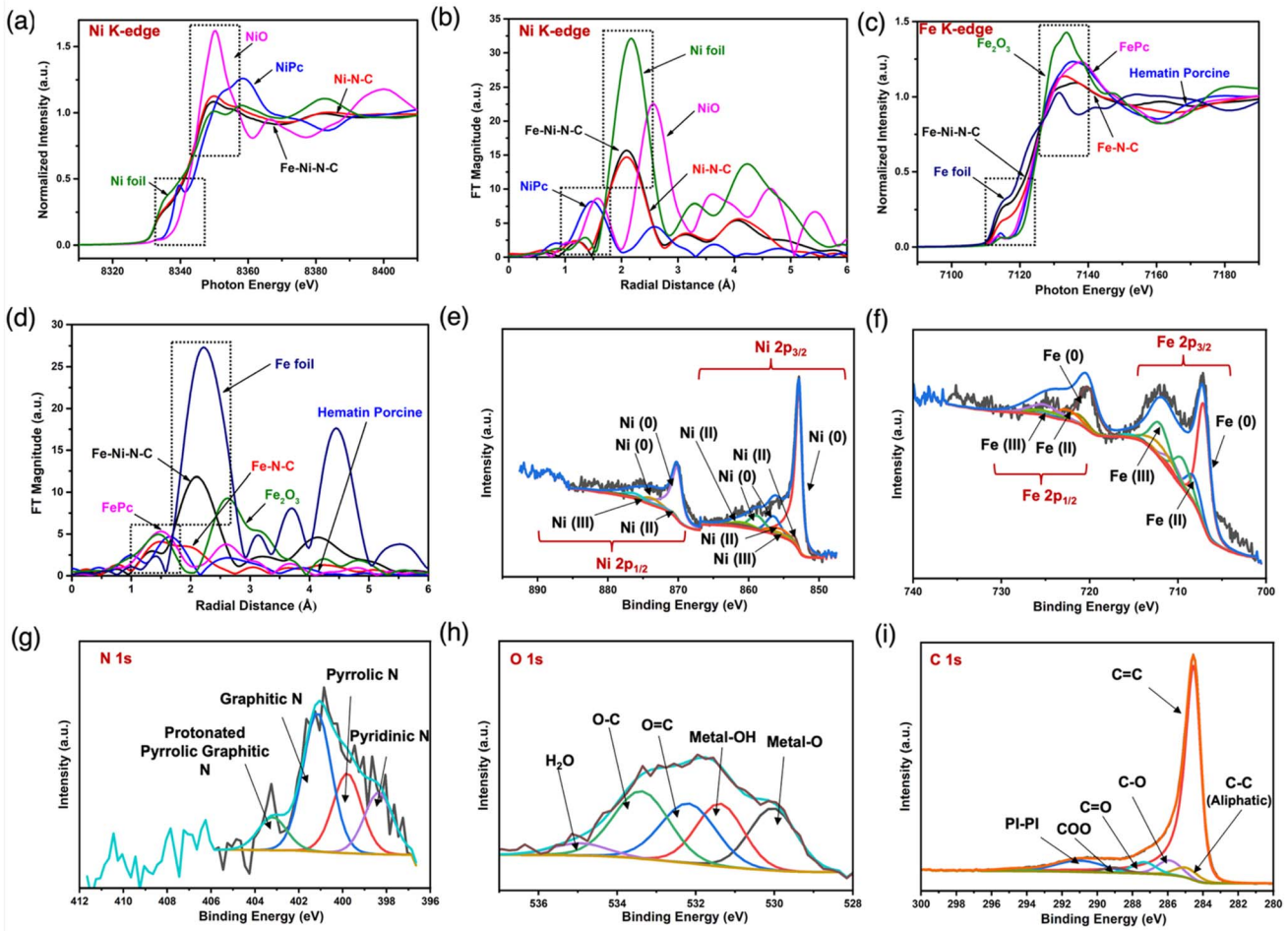

Fig. 3 Structure identification of Fe–Ni nanostructures using XPS and XAS. (a) XANES of Ni k-edge; (b) EXAFS of Ni k-edge; (c) XANES of Fe k-edge; (d) EXAFS of Fe k-edge; (e) high-resolution XPS of Ni 2p spectra; (f) high-resolution XPS Fe 2p spectra; (g) high-resolution XPS of N 1s spectra; (h) high-resolution XPS of O 1s spectra; and (i) high-resolution XPS of C 1s spectra.

intermetallic bonds. In contrast, NiPc and FePc display a prominent feature near 2.6 Å arising from multiple ligand scattering, which is absent in Fe–Ni/N–C due to structural disorder and the embedding of metal centers within defective carbon planes. Collectively, XANES, EXAFS, and XPS analyses confirm that a small portion of the Fe–Ni/N–C heterostructure contains mixed Fe and Ni single-atom sites coordinated with pyrrolic, pyridinic, and graphitic nitrogen as well as oxygen functionalities, while the majority features predominant Fe–Ni intermetallic coupling.

In addition to probing the metal coordination environment, we also analyzed the carbon structure in Fe–Ni/N–C using XPS. The results (Fig. 3i) show that carbon, comprising approximately 90 atomic %, is predominantly present as graphitic sp^2 C–C bonds at 284.4 eV (73%), while the remaining 27% corresponds to C–O (285.9 eV), aliphatic C–C (284.9 eV), C═O (287.3 eV), and COO (289.0 eV) species. This composition indicates that the carbon framework is largely well-ordered and graphitic yet retains a small fraction of disordered and heteroatom-functionalized sites that may facilitate electronic conductivity and active site stabilization. These structures are better described as turbostratic carbon, rather than "graphene," as they contain both ordered and disordered carbon phases. This finding is consistent with HRTEM images (Fig. S10), which show that most of the carbon is in an ordered graphitic form, with some disordered regions present. Additionally, Raman spectroscopy (Fig. S11) further supported this classification by detecting a strong 2D band, indicative of graphitic structures with some disorder. An important aspect of our study is that we also synthesized the same material without any metal to investigate the coordination environment between the heteroatoms and metals, and to determine whether the metals play a role in stabilizing these heteroatoms after photothermal pyrolysis. XPS data (Fig. S12) revealed a significant decrease in the atomic percentage of N, from 2.1% to 1.2%, and O, from 3.3% to 2.2%. This suggests that during synthesis, a coordination environment forms between the metals and heteroatoms, which serves to stabilize both metal and heteroatoms during the photothermal pyrolysis process. In contrast, the absence of metal–heteroatom bonds leads to a greater loss of N and O from the material. These heteroatoms could potentially enhance the electrocatalytic performance, as reported in numerous studies.

It is important to note that XPS analysis (Fig. S13) confirmed that the Cl ligands were fully removed during the pyrolysis process.

OER electrocatalysis performance and active site analysis

Since single metal Ni is a well-established catalyst for oxygen evolution,[34,35] we focused on optimizing our Fe–Ni bimetallic nanostructure catalyst. This catalyst was subsequently used as the anode in the MEA. To optimize the Fe-to-Ni ratio on the turbostratic carbon, OER tests were performed in a 1 M KOH electrolyte using a three-electrode electrochemical cell, with a glassy carbon as the substrate of working electrode, onto which the as-synthesized catalyst ink was drop-cast. We first kept the Fe/Ni ratio at 1 : 1 and varied the total weight percentages of Fe and Ni, using overpotential at 10 mA cm^2 as the key performance metric (Fig. 4a). The 10 wt% Fe–Ni sample exhibited the lowest overpotential (190 mV), whereas increasing the loading to 20 wt% raised the overpotential to 310 mV. This decline in OER performance is likely due to the growth of larger nanoparticles on turbostratic carbon. To confirm that the performance difference arises primarily from particle size rather than compositional heterogeneity, we examined TEM images before and after HCl washing. The results (Fig. S14) indicate that HCl treatment effectively removes large and medium-sized particles, while particles with an average size of ~28 nm remain mostly intact. This supports the conclusion that particle size is the predominant factor governing the observed OER activity. XPS analysis (Fig. S15) further revealed that increasing metal loading induces greater disorder in the sp^2 structure of turbostratic carbon and promotes oxide formation. This indicates that chemical composition also plays a critical role, with an optimal Fe–Ni content of 10 wt% (4 at%) in Fe–Ni nanostructures. Building on this, we systematically varied the Fe to Ni ratio at a fixed 10 wt% loading and observed that even small changes in Fe content significantly affect OER activity (Fig. 4b), as reflected in the overpotential. These results highlight the combined importance of particle size and precise composition in achieving optimal catalytic performance. González-Ingelmo *et al.* also observed a similar trend in their study of NiFe catalysts on graphene, where reducing Fe content and increasing Ni proportion in Fe/Ni led to improved OER performance. It is worth noting that the introduction of carbon as a metal support is a key factor, as the interaction between the metal and carbon can modify the catalyst's behavior. Carbon provides conductivity, which directly impacts electrocatalytic performance and efficiency, potentially enhancing or lowering the overall performance. Based on these observations, we speculate that the high overpotential observed in the 0.1 Fe/Ni sample must be due to the formation of large nanoparticles with disrupted carbon moieties, which are likely inactive for

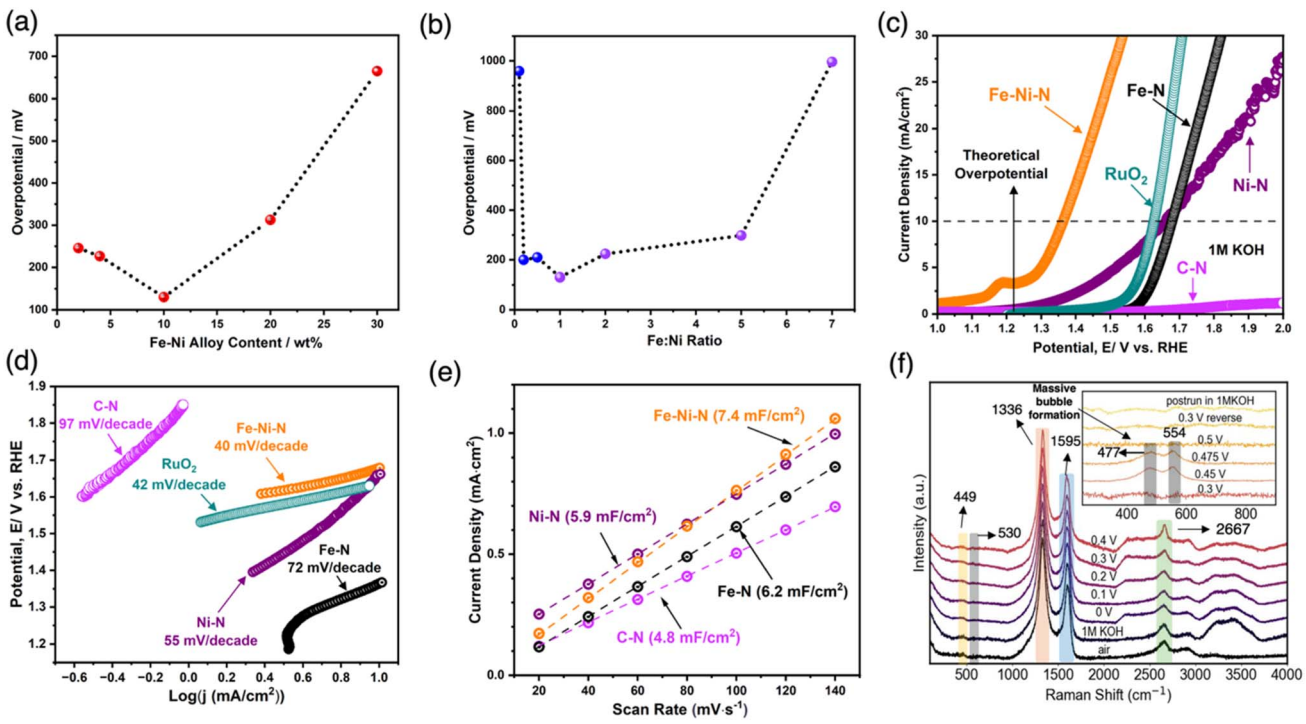

Fig. 4 Electrocatalytic performance of OER in 1 M KOH at 25 °C and *in situ* Raman spectroscopy. (a and b) Key electrochemical parameters are affected by the active surface layer chemical composition. Overpotential of the corresponding OER region, calculated based on the geometric current density of 10 mA cm^{-2}, as a function of Fe to Ni ratio content at different weight percentages; (a) overpotential as a function of Fe to Ni ratio content at varying wt%; (b) overpotential as a function of Fe to Ni ratio content (wt%) changes on a fixed 10 wt% Fe–Ni; (c) polarization curve calculated based on geometric current density, with a metal loading of 10 wt% for each catalyst except metal free C–N; (d) corresponding Tafel plot; (e) electrochemical surface area; and (f) *in situ* Raman spectroscopy of 10 wt% hierarchical Fe–Ni nanostructures at different potentials, using a 633 nm wavelength laser to detect the spectra. The inset displays the spectral changes of Fe and Ni in the Raman shift range from 200 to 800 cm^{-1}, observed between 0.45 and 0.50 V *vs.* Ag/AgCl.

OER. Notably, the 33 nm pore structure in our sample facilitates the transport of O_2 and H_2O to and from the active sites, thereby improving both OER and MEA performance. Nevertheless, plotting the OER activity against the Fe/Ni ratio in the catalyst layer (Fig. 4a and b) reveals that a higher Fe/Ni ratio at 10 wt% reduced the performance of the active sites. This aligns with the findings of Todoroki *et al.*, who emphasized that both the Fe/Ni ratio and the catalyst's ability to generate a well-formed layer with a large surface area are key factors in achieving optimal OER performance.[36]

After confirming that the 1 : 1 Fe/Ni ratio with 10 wt% was the optimal catalyst for our system, we conducted a detailed analysis of its OER activity and compared it with individual 10 wt% Fe and 10 wt% Ni metal nanostructure samples (Fig. 4d and e). The individual hierarchical Fe and Ni nanostructures were synthesized using the same method as the Fe–Ni bimetal. HAADF-STEM (Fig. S16) was used to confirm the distribution of single metal atoms, clusters, and small nanoparticles within the turbostratic carbon matrix. Additionally, XPS analysis (Fig. S17 and S18) of the same sample confirmed the chemical composition of the surface elements. This distribution also highlights the versatility of our synthesis method, which can produce hierarchical metal nanostructures (range of metal cluster sizes, from single atoms to small nanoparticles), including isolated metal atoms, beyond just alloy compositions. The Fe–Ni catalyst required a potential of 1.36 V *vs.* RHE (Fig. 4d) to reach a geometric current density of 10 mA cm^{-2}. This low overpotential further indicates the high intrinsic activity of the catalyst, which is additionally supported by electrochemical impedance spectroscopy (EIS). The Nyquist plots (Fig. S19) reveal a clear decrease in charge-transfer resistance with increasing potential. Consistently, the catalyst exhibits a low Tafel slope of 40 mV per dec (Fig. 4e), confirming its superior intrinsic activity. The overpotential and Tafel slope values of the catalyst (with 10 wt% metal loading) underscore a defining characteristic of our surfaces-exceptional electrocatalytic performance that surpasses many previously reported materials (Table S1), particularly in terms of intrinsic OER activity.

In comparison, the individual porous nanostructures of Fe–N–C, Ni–N–C, and metal-free porous C–N required 1.53 V, 1.67 V, and 1.75 V, respectively, with corresponding Tafel slopes of 55, 72 mV, and 97 mV per dec to achieve the same current density (Fig. 4c and d). The higher overpotentials for the individual metal and metal-free catalysts indicate that the synergistic interaction between Fe and Ni in Fe–Ni/N–C generates more active sites than either metal alone or without metal. The number of electrochemically active sites is reflected by the electrochemically active surface area (ECSA). To estimate the ECSA, the double-layer capacitance (C_{dl}) was obtained (Fig. 4e) from cyclic voltammetry at various scan rates within a non-faradaic potential window, and the resulting current densities were linearly fitted (Fig. 4e). The Fe–Ni/N–C catalyst exhibited the highest C_{dl} (7.4 mF cm^{-2}), followed by Fe–N–C (6.2 mF cm^{-2}), Ni–N–C (5.9 mF cm^{-2}), and C–N (4.8 mF cm^{-2}). According to the literature, ECSA is proportional to C_{dl}, with the surface area estimated from C_{dl}/C_s, where $C_s = 40$ μF cm^{-2} (0.04 mF cm^{-2}) in alkaline media. Accordingly, the calculated ECSAs are approximately 185, 155, 148, and 120 cm^2 for Fe–Ni–N–C, Fe–N–C, Ni–N–C, and C–N, respectively. Furthermore, based on the ECSA-normalized current density, Fe–Ni/N–C exhibits a markedly higher intrinsic activity than the other catalysts, consistent with its lowest Tafel slope. This superior performance is further corroborated by the measured and calculated mass activity, ECSA-normalized current densities, and turnover frequency values (Fig. S20), which show the same trend. To validate the robustness of the rapid photothermal pyrolysis method, three independent synthesis batches ($n = 3$) were conducted under identical conditions. The catalysts exhibited consistent metal loadings (±0.5 wt%), similar particle size distributions, and less than 5% variation in OER overpotential at 10 mA cm^{-2} (Fig. S21), confirming excellent reproducibility. To evaluate scalability, the catalyst yield per batch and energy consumption were estimated based on the power input and synthesis duration. The energy consumption for the photothermal process was approximately 0.017 kWh g^{-1}, calculated for a 300 W light source operated for 100 s, producing 0.5 g of catalyst. This value is substantially lower than that of conventional furnace pyrolysis (0.2–0.5 kWh g^{-1}), demonstrating the superior energy efficiency of the method. Although large-scale implementation remains a future objective, these results collectively underscore the reproducibility, energy efficiency, and strong potential of the rapid photothermal pyrolysis approach for high-throughput catalyst production.

Our hierarchical Fe–Ni nanostructures on porous carbon show impressive OER activity, but the role of single atoms and clusters remained a puzzle. To probe this, we selectively removed clusters and isolated atoms by washing the Fe–Ni structure with 2 M HCl for 24 h. HAADF-STEM (Fig. S22) confirmed their complete removal, leaving only small nanoparticles. Surprisingly, LSV and Tafel plots showed minimal changes (overpotential shifted only from 130 mV to 135 mV; Tafel slope slightly increased to 44 mV per dec). This striking result reveals that, although single atoms and clusters are often confirmed as the ultimate active sites in electrocatalysis, in our system, they play only a minor role. The real OER performance stems from the Fe–Ni intermetallic nanoparticles, where synergy between metals, one binding reactants, the other stabilizing intermediates, drives superior activity. This counterintuitive finding underscores that not all notable single-atom catalysts dominate the reaction.

The above experiment confirmed that the Fe–Ni synergy enhances OER performance and activates the primary catalytic sites. The next key question concerns the relative contributions of Fe and Ni, and why the Fe–Ni catalyst exhibits superior OER activity compared to Fe–N–C and Ni–N–C, despite their similar structural features and metal size distributions. To confirm the reaction pathway and to identify the active sites, we conducted *in situ* Raman spectroscopy on the Fe–Ni/N–C catalyst under the working conditions (Fig. 4f). A series of Raman spectra for a Fe–Ni film deposited on a glassy carbon electrode (GCE) substrate and immersed in 1 M KOH, recorded at various applied potentials (*vs.* Ag/AgCl) during an oxidation sweep (Fig. 4f). The observed spectral features and their potential-dependent changes were consistent with the transformation of $Ni(OH)_2$ to NiOOH, beginning at a potential of 0.45 V *vs.* Ag/AgCl. The

band at 449 cm^{-1} was attributed to $Ni(OH)_2$, which exhibited Ni–O vibrational modes in the range of 445 to 465 cm^{-1}. Additionally, a band at 530 cm^{-1} was observed, which was associated with disordered $Ni(OH)_2$.[37,38] At higher Raman shifts, the bands between 3250 and 3271 cm^{-1} were attributed to O–H vibrations of $Ni(OH)_2$. Given the broader range of Raman shifts between 3100 and 3600 cm^{-1}, these bands could also be related to the O–H stretch of hydrogen bond water, which was commonly observed in this region.[39–41] The pair of bands at 477 and 554 cm^{-1}, observed with high intensity between 0.45 V and 0.47 V *vs.* Ag/AgCl, were ascribed to Ni–O vibrations in NiOOH. We did not attempt to distinguish or analyze the specific contributions from the γ and β-NiOOH phases, which are both expected to exhibit bands in this region. At 0.49 V, we also observed a NiOOH peak but slightly shifted to lower wavenumbers, though it was of very low intensity, and nearly negligible at 0.5 V. This reduction in intensity was likely due to the formation of intense oxygen bubbles during the OER, which interfered with Raman scattered light collection. These bubbles were difficult to remove and may have obstructed the laser from effectively probing the catalyst surface. For Fe, the bands in the 650 to 720 cm^{-1} range showed changes in intensity with varying potential and were too weak. The identification of the observed bands was complicated by the numerous possible Fe oxide and oxyhydroxide phases, many of which have similar structures. The bands in the 650 to 720 cm^{-1} range were likely associated with Fe_3O_4, Fe_2O_3, and FeOOH, respectively.[42] It is worth noting that no distinct $NiFe_xO_x$ features were observed in the Raman spectra during OER. This absence may result from the strong intensity of Ni-related peaks, which could mask subtle spectral changes associated with $NiFe_xO_x$ formation. However, given the Fe–Ni intermetallic bonding in our catalyst, the presence of such species during OER cannot be ruled out.[43] Notably, after OER, when measured in KOH without applied potential, the Raman peaks at 477 and 554 cm^{-1} disappeared, suggesting that the intermediate species formed during OER were potential-dependent and confirming the reversible transformation between $Ni(OH)_2$ and NiOOH under varying potentials. During our *in situ* observations, we did not observe any significant changes in the D, G, or 2D peaks of the turbostratic carbon support compared to the pristine catalyst measured at room temperature. This suggested that the carbon structure remained largely intact throughout the potential-dependent measurements. However, at potentials greater than 0.47 V *vs.* Ag/AgCl, high OER activity led to extensive bubble formation, hampering our ability to record a clear Raman spectrum. Nevertheless, our Raman spectroscopy results lead to three key conclusions: (a) The Fe–Ni nanostructure is highly disordered, consistent with our XAS results and previous reports on amorphous metal oxides in OER catalysis. Raman likely captured local Ni–O features not resolved by EXAFS, which mainly probes Ni's short-range coordination,[44–46] (b) NiOOH intermediates formed during the OER process, but the Raman peaks shifted to lower wavenumbers, indicating that the structure was not purely NiOOH but rather incorporated Fe species, and (c) FeOOH typically exhibits distinct bands at ∼385, 480, and 550 cm^{-1}; however, in mixed FeNiOOH, the Fe signals are weak and often masked by stronger Ni vibrations. Consequently, Fe–O and Ni–O vibrations couple to form composite modes instead of distinct peaks.

Based on both spectroscopic and electrochemical observations, and drawing on the work of Bell,[47] Myers, and Hermann,[48] Boettcher,[44] and our previous studies[6,21] on Fe- and Ni-doped N–C catalysts, two plausible explanations emerge for the exceptional OER activity of Fe–Ni systems in alkaline media. In Fe–N–C and Ni–N–C, the dominant active phases under OER conditions are FeOOH and NiOOH, respectively, as confirmed by our earlier work and others. In these monometallic systems, the active sites are straightforward: Fe in Fe–N–C and Ni in Ni–N–C. Because OER intermediates bind too strongly to Fe and too weakly to Ni, Ni–N–C exhibits slightly higher activity, consistent with previous reports.[47,49] The situation becomes more complex in bimetallic Fe–Ni systems. Although the formation of NiOOH intermediates is well established, the precise catalytic roles of Fe and Ni depend strongly on their atomic configuration. When Fe is incorporated into the subsurface or bulk of $Ni–OH_x$, it can increase the OER overpotential by further weakening Ni's oxygen affinity.[50] In contrast, Fe dimers adsorbed on $Ni–OH_x$ may serve as the primary active sites, where Fe stabilizes oxyl radicals on Ni through exchange interactions and Ni promotes O–O coupling.[51] Based on our experimental observations, the former scenario is more likely operative in our system. Two lines of evidence support this conclusion: (a) XPS analysis reveals higher Fe oxidation states than Ni, consistent with Ni's greater electron affinity, withdrawing electron density from oxygen sites. Consequently, Fe doping lowers the average Ni oxidation state compared to pure NiOOH, suggesting that Ni cations remain the primary active centers in (Fe, Ni) OOH, in agreement with other reports; and (b) no evidence of a lattice oxygen mechanism (LOM) is observed, as LOM generally compromises structural stability,[52] contrary to our MEA durability results. This further suggests that Fe doping stabilizes adsorbed oxygen species and suppresses lattice oxygen radical character, particularly when Ni serves as the dominant active site. It is important to note, however, that Fe–Ni/N–C catalysts may not strictly follow the same behavior described by Bell and co-workers,[53] where Fe serves as the primary active site. Finally, we cannot rule out that N and C coordination influences the Fe–Ni interaction and active-site structure, underscoring the need for further *operando* and theoretical studies to fully elucidate their roles in enhancing OER activity.

Although metal clusters and single atoms are not the major species after OER cycles, previous reports, including our own work, identify active sites for isolated metal Ni and Fe atoms through spectroscopic and density-functional theory (DFT) calculations.[6,32] These sites may also play some role in the current system, as reflected in the LSV measurements. Thus, we first performed DFT calculations to compare catalytic OER cycles on metal clusters. Four model systems were constructed, including monometallic Fe_4 and Ni_4 clusters and bimetallic Fe_3Ni and Ni_3Fe clusters. Similar to the model used in our previous work,[21] a graphene sheet was used as the support, of which two carbon atoms were removed to create a divacancy defect[54] to accommodate the supported metal clusters

(Fig. S23a). To identify the most stable surface structures under electrochemical conditions, Hansen *et al.*[55] constructed surface Pourbaix diagrams based on DFT calculations and found that Ni (111) would be covered by hydroxyls until at least U_{RHE} = 1.4 V. Using a similar strategy, we estimated the stability of hydroxylated metal clusters for all four model systems ($M_4(OH)_3 \rightarrow M_4O_3 + 3H^+ + 3e^-$) and determined that Fe_3Ni/C, Ni_3Fe/C, and Ni_4/C similarly maintain their $M_4(OH)_3$ phase up to U_{RHE} of ~1.4 V, while Fe_4/C may be oxidized to Fe_4O_3 at potentials above U_{RHE} of ~1 V. For the sake of consistency, the calculations, therefore, treated all model systems in their hydroxylated state. As shown in Fig. S23a, all M_4 clusters feature the tri-fold hollow site as the active site.[56–58] Fig. S23b shows the calculated free-energy profiles at both U_{RHE} = 0 and 1.23 V, while Fig. S23c compares the free energy change of each oxidation step at U_{RHE} = 1.23 V. In alkaline media, the reaction pathway of OER starts with the oxidative binding of OH^- to the hollow site to form *OH, which undergoes attack by another OH^- ion to produce *O and water in the second oxidation step. The third oxidation step in the standard alkaline OER mechanism involves the nucleophilic attack of *O by OH^- to form *OOH, which is often the potential-determining step.[59–61] However, as found in our previous study,[21] the third oxidation step on all four hydroxylated metal clusters, instead, occurs more easily by removing a proton from a neighboring metal hydroxyl group to generate another water molecule and $M_3(OH)_2M'O$ (denoted as (o)O in Fig. S23a. In the bimetallic case, this second proton abstraction can take place on either metal, and our DFT calculations showed that oxidation of a neighboring Fe atom is more preferable than that of a Ni atom by 0.3 and 0.4 eV for Ni_3Fe/C and Fe_3Ni/C, respectively. This suggests a potential synergistic effect in the bimetallic clusters. The stabilization of the oxidized intermediates *O and (o)O shifts the potential-determining step to the last oxidation step, which consumes OH^- ion to regenerate the active-site ensemble and release O_2.

As OER progresses, metal nanoparticles become the dominant species with oxidized surface layers manifesting as oxyhydroxides under alkaline anodic conditions. Previous studies identified β-NiOOH phase to be the active phase and found that Fe doping up to ~30% enhances OER reactivity.[49,62–64] Moreover, based on thermodynamic Wulff constructions, solvated low-index facets were estimated to constitute ~70% of β-NiOOH surface.[65] We therefore focused on the (0001) facet of Fe-doped β-NiOOH and constructed three models of varying Ni/Fe ratio, $Ni_3FeO_8H_4$ (referred to below as Ni_3Fe_1–OOH), $Ni_2Fe_2O_8H_4$ (Ni_2Fe_2–OOH), and $NiFe_3O_8H_4$ (Ni_1Fe_3–OOH), to investigate the effect of higher levels of Fe doping on OER activity (Fig. 5). For these systems, the DFT+*U* approach was adopted. The Hubbard *U* values were computed using the linear response theory and ranged from 5.76 to 6.75 V for Ni and from 4.45 to 5.04 V for Fe (Table S2).[66] These values were then averaged for the DFT+*U* calculations to ensure consistent energetics. Under alkaline conditions, the OER mechanism starts with the attack of a surface oxygen atom by OH^- to form *OOH (R1), which reacts with another OH^- ion to produce *OO and water (R2). The release of O_2 generates an oxygen vacancy (denoted as *) on the surface (R3), which binds an OH^- ion to form *OH (R4). The last oxidation step with another OH^- ion produces water and regenerates the *O active site (R5). At U_{RHE} = 1.23 V, R1 was found to be the potential-determining step, similar to previous reports,[47,64,67] for the $Ni_3FeO_8H_4$ and $Ni_2Fe_2O_8H_4$ systems. The reaction free energy is 0.53 eV for $Ni_3FeO_8H_4$ and increases to 0.64 eV for $Ni_2Fe_2O_8H_4$. As Fe level further increases, the free-energy cost of R1 reduces to 0.56 eV for $NiFe_3O_8H_4$, but the release of oxygen from surface becomes much more difficult, with a reaction free energy of 0.72 V (*c.f.*, 0.50 eV in $Ni_3FeO_8H_4$), making R3 as the potential-determining step. For these model systems, higher levels of Fe doping (>48 wt%) present a detrimental effect, consistent with the experimental observations (Fig. 4). Though these results complement previous computational studies with lower levels of Fe doping in acidic conditions, a more thorough study of the effect of different facets, other oxyhydroxide phases, and using higher levels of quantum-chemical theory may be necessary to provide a more complete mechanistic picture.

Evaluation of Fe–Ni/N–C catalysts in MEA configuration for practical water splitting

We finally constructed an MEA cell using Fe–Ni for practical water electrolysis in alkaline conditions. The catalysts were deposited onto non-woven carbon paper, which served directly as the anode. The cathodic membrane (NiMo) and the anion exchange membrane (AEM) were commercially sourced. Remarkably, this custom-made MEA water electrolysis cell (Fig. 6a and S24) achieved a stable current density of 100 mA cm^{-2} at 80 °C with a voltage of 1.75 V in a 1 M KOH solution. The operating voltage for the FeNi alloy || commercial NiMo cell was notably lower than those of previously reported electrocatalyst-based symmetrical cells in alkaline electrolytes.[68–72] To evaluate faradaic efficiency (FE), we conducted a water-drainage experiment in an alkaline electrolyte. By collecting the generated H_2 and O_2 gases during water splitting and plotting their volumes over time, we found that the H_2 to O_2 ratio was approximately 2 : 1, which matches the theoretical value. From this, we calculated the FE to be 99%. This indicated that no side reactions occurred during water splitting. Additionally, the cell showed exceptional stability (Fig. 6b), maintaining a consistent current density of 100 mA cm^{-2} at 1.75 V for 50 hours without voltage decay in the alkaline pH. A slight decrease in current density was observed after the initial hours of operation. To investigate this, the morphology of the hierarchical Fe–Ni nanostructure was examined using STEM-EDX and EELS after 50 h in the MEA (Fig. 6c and S25). The analysis revealed the complete absence of single atoms and clusters (<1 nm) on the carbon support, suggesting that the minor drop in current density after ~49 h is likely due to the loss of these species. As a minor population in our structure, single atoms and small clusters degrade faster than nanoparticles because of their higher surface energy and lower coordination numbers, leading to dissolution, aggregation, or migration, whereas the dominant nanoparticles remain largely stable. At low overpotentials (10 mA cm^{-2}), the intrinsic catalytic activity dominates; at higher current densities (100 mA

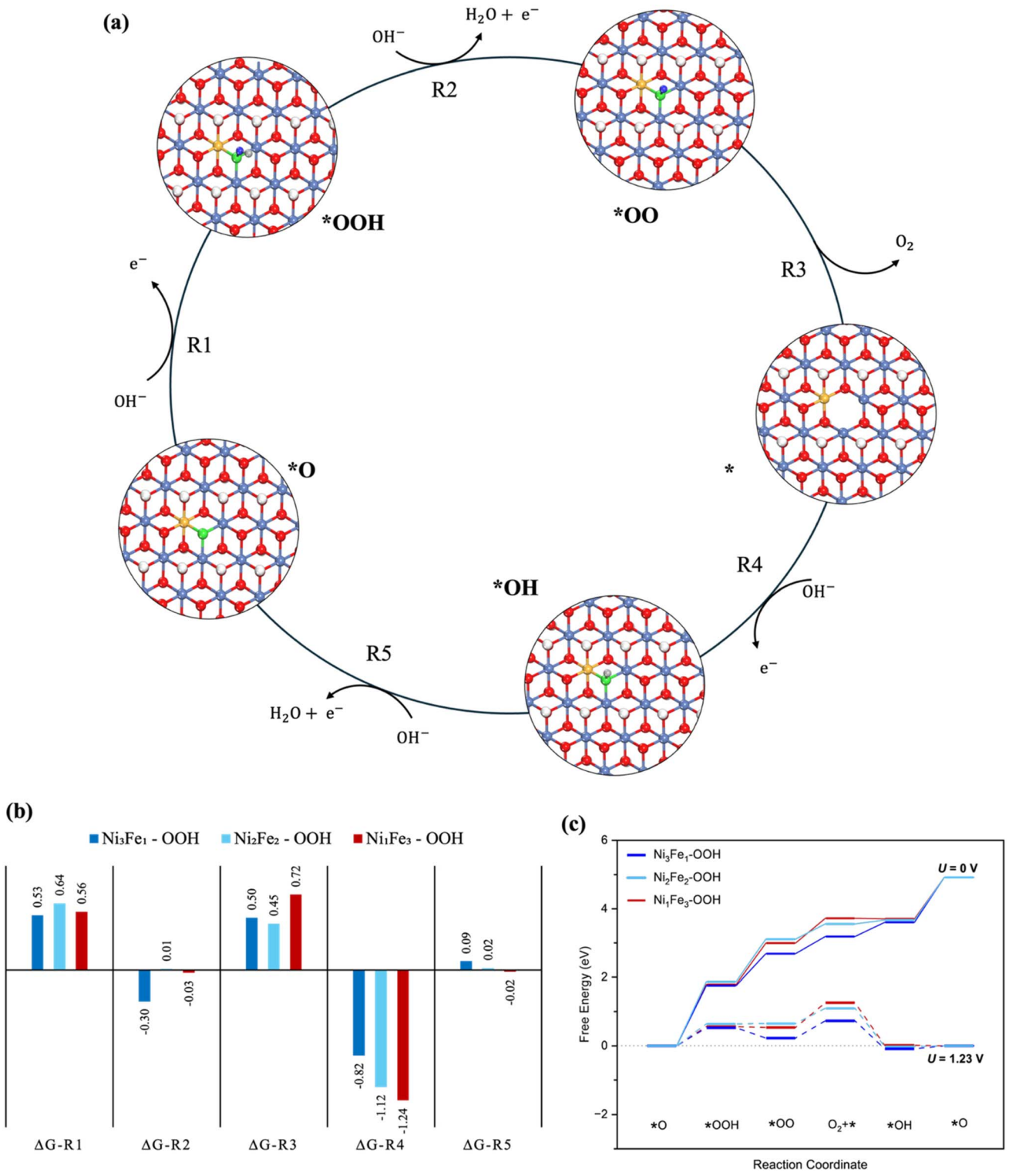

Fig. 5 The OER reaction in alkaline media on the (0001) facet of β-NiOOH. (a) Schematic representation of the OER mechanism on Fe-doped β-NiOOH [Ni_3Fe_1–OOH], illustrating the oxidation and site-regeneration steps involving *O, *OOH, *OO, *, and *OH species. Surface oxygen, hydrogen, nickel, and iron atoms are shown in red, white, light blue, and yellow, respectively. The active site oxygen, adsorbed oxygen, and hydrogen are shown in light green, dark blue, and off-white, respectively; (b) comparison of free energies for individual OER steps for the different nanoparticles at an applied potential of $U_{RHE} = 1.23$ V (c) free-energy diagram for the OER process at an applied potential of $U_{RHE} = 0$ V (solid line) and 1.23 V (dashed line).

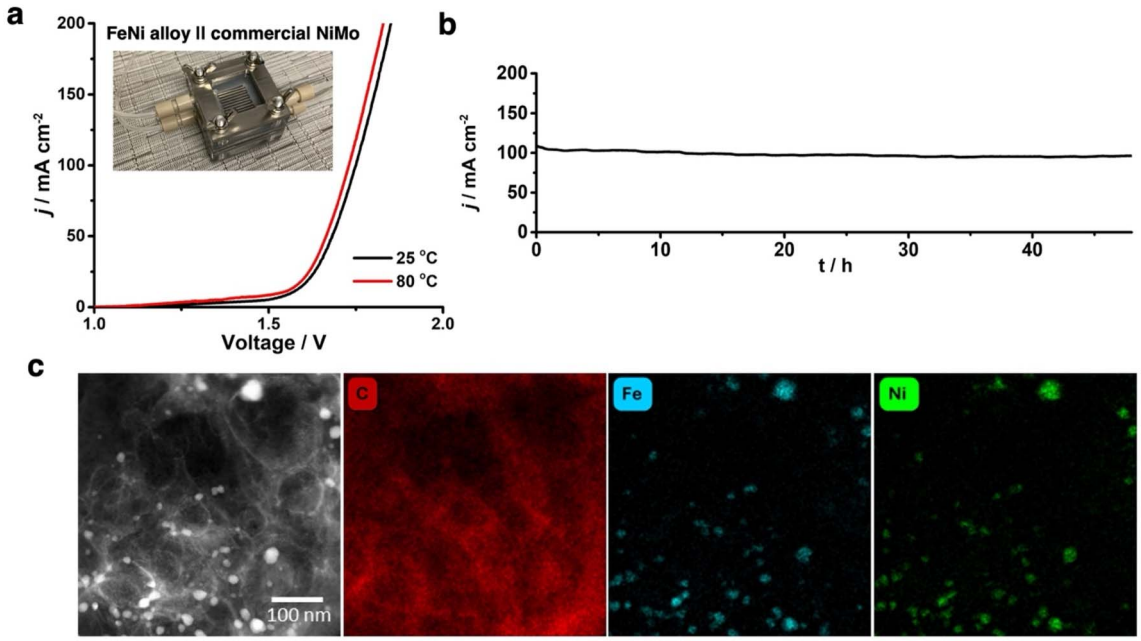

Fig. 6 Water splitting performance using MEA, stability, and morphology. (a) Electrolysis test using an MEA comprising an alkaline membrane with two symmetric electrodes: hierarchical Fe–Ni/C (anode) and commercial NiMo/C (cathode). Performance was measured at 85 °C and 25 °C, respectively, under ambient pressure with 1 M KOH circulating through the anode and cathode. The inset shows a photographic image of the electrolyzer; (b) the durability of the electrolyzer at a constant current density of 100 mA cm^{-2}; (c) HAADF-STEM image of the anode after 50 hours of the durability test showing no change in the hierarchical structure albeit the absence of single atoms and corresponding EDS elemental maps showing no Fe or Ni in regions with no nanoparticles.

cm^{-2}), mass transport limitations, increased ohmic resistance, and gas bubble accumulation contribute to the higher applied potential. Additionally, concentration gradients and local electrolyte depletion near the catalyst surface can hinder reaction kinetics, further increasing overpotential. Nevertheless, our synthesized hierarchical Fe–Ni metal catalysts demonstrated exceptional activity, surpassing most reported electrocatalysts for overall water splitting in alkaline conditions. They also exhibited high efficiency in converting electrical energy into chemical energy, further reinforcing the robustness of our catalyst system. This offers strong confidence in its long-term performance and potential for future applications.

Conclusions

In summary, we demonstrated a successful one-pot synthesis of Fe–Ni nanostructures, in which the majority of the active species consist of Fe–Ni alloy nanoparticles, along with isolated Fe and Ni single metal atoms and Fe–Ni metal clusters dispersed on a porous turbostratic carbon support. The synthesis was achieved using BBCP templates followed by rapid photothermal pyrolysis. The resulting nanostructures were comprised of isolated metal atoms, clusters, and small nanoparticles, which were well-distributed throughout the carbon matrix and predominantly decorated the graphitic planes, with some exhibiting oxide core–shell structures. The optimized Fe–Ni/N–C catalyst exhibited high electrocatalytic activity toward OER, showing an overpotential of 130 mV (*vs.* RHE) at a geometric current density of 10 mA cm^{-2} in 1 M KOH electrolyte, and a Tafel slope of 40 mV per dec. A range of spectroscopic and microscopic techniques, along with theoretical calculations, including *in situ* and *ex situ* Raman spectroscopy and *ex situ* XPS, to gain a deep understanding of the catalytic process. Our findings show that *in situ* Raman spectroscopy identifies NiOOH as a key active intermediate, and DFT calculations indicate that while moderate Fe incorporation enhances OER activity, excessive Fe doping ultimately hinders performance by making oxygen release the rate-determining step. The results of this study emphasize the critical role of high-valent Ni and Fe species in driving OER activity. While Fe in the bulk may not act as the primary active site, its presence near the catalyst surface within a few atomic layers in the nanosheet-structured material helps stabilize the adsorption of OER intermediates on Ni. These findings indicate a synergistic interaction between Ni and Fe during OER. Moreover, the distinct morphology of our catalyst appears to enhance this synergy, contributing to the superior OER performance observed in this system. Additionally, the alkaline MEA with the as-synthesized Fe–Ni/N–C electrocatalyst as anode and the commercial NiMo catalysts as cathode were employed for electrolysis of water splitting, achieving 100 mA cm^{-2} at 1.75 V in 1 M KOH electrolyte at 80 °C. The combination of high surface area and diverse metal nanostructure sizes in a porous framework positions this material as a promising candidate for use as an anode electrode in MEA for OER. This study provides key insights for designing non-platinum electrocatalysts, offering a route to efficient, durable, and cost-effective materials for water electrolysis, while our synthesis approach simplifies

hydride metal formation and ensures a high density of earth-abundant metal atoms before large nanoparticle clusters form.

Author contributions

The concept and experimental design were developed by Dipankar Saha, Nianqiang Wu, and James J. Watkins. Dipankar Saha performed all experimental work and analyzed the data with input from Peng Bai, Nianqiang Wu, and James J. Watkins. Chaoyung Tang contributed to MEA measurements and calculations; Pulkit Jain and Zhu Chen to *in situ* Raman; Cheng-Jie Yang, Chung-Li Dong, and Chi-Liang Chen to XANES and EXAFS; Richard Webster and Richard Tilley to STEM; and Javed Khan and Peng Bai to theoretical calculations. All authors contributed to discussions of the results. The manuscript was written by Dipankar Saha, with the theoretical calculations section prepared by Javed Khan, and revised with feedback from all co-authors.

Conflicts of interest

Dipankar Saha, Chaoyun Tang, Nianqiang Wu, and James J. Watkins have filed for a provisional U.S. patent covering the synthesis process and application described in this manuscript.

Data availability

The data supporting this article have been included as part of the supplementary information (SI). Supplementary information: a detailed description of materials and methods, additional SEM, STEM, and TEM images, XPS, Raman and XAS analysis, and additional DFT analysis and MEA fabrication schematic. See DOI: https://doi.org/10.1039/d5sc05330g.

Acknowledgements

The authors would like to acknowledge the Penn State Materials Characterization Lab for providing access to the XPS instrument, and to Robert Hengstebeck (Bob) for his valuable discussions on sample preparation and measurement. They also acknowledge the facility services for electron microscopy and spectroscopy at the Department of Polymer Science and Engineering, as well as the Institute of Applied Sciences at the University of Massachusetts, Amherst, USA, specifically Cedric Bobst, for helping with ICP-MS measurement. Special thanks are extended to the Watkins group members, particularly Dr Takumi Uchiyama, Karan Sagar, Connor Witt, and Varun Pande, as well as the Wu group members, for their fruitful discussions. Electron microscopy was conducted at CCEM-McMaster University, a national facility supported by NSERC Canada (Dr Carmen Andrei). The authors acknowledge the technical support provided by Microscopy Australia at the Electron Microscope Unit, Mark Wainwright Analytical Centre (UNSW Sydney), and appreciate the beamtime allocated by the National Synchrotron Radiation Research Center (Taiwan) for the XAS measurements. The authors gratefully acknowledge financial support from the US Army Research Laboratory (under the National Center for Manufacturing Sciences, award number HQ0034-15-2-0007, and Expeditionary Maneuver Support award number W911QY1990011), as well as the Office of Naval Research (under LIFT award number N000142190010). ChatGPT was utilized solely for language polishing and was not involved in writing the original manuscript.

References

1 Y. Guo, M. Wang, Q. Zhu, D. Xiao and D. Ma, Ensemble effect for single-atom, small cluster and nanoparticle catalysts, *Nat. Catal.*, 2022, **5**, 766–776.
2 X. Sun, S. R. Dawson, T. E. Parmentier, G. Malta, T. E. Davies, Q. He, L. Lu, D. J. Morgan, N. Carthey, P. Johnston, S. A. Kondrat, S. J. Freakley, C. J. Kiely and G. J. Hutchings, Facile synthesis of precious-metal single-site catalysts using organic solvents, *Nat. Chem.*, 2020, **12**, 560–567.
3 W. M. H. Sachtler and R. A. V. Santen, in *Advances in Catalysis*, ed. D. D. Eley, H. Pines and P. B. Weisz, Academic Press, 1977, vol. 26, pp. 69–119.
4 L. Liu and A. Corma, Metal Catalysts for Heterogeneous Catalysis: From Single Atoms to Nanoclusters and Nanoparticles, *Chem. Rev.*, 2018, **118**, 4981–5079.
5 C. Dong, Z. Gao, Y. Li, M. Peng, M. Wang, Y. Xu, C. Li, M. Xu, Y. Deng, X. Qin, F. Huang, X. Wei, Y.-G. Wang, H. Liu, W. Zhou and D. Ma, Fully exposed palladium cluster catalysts enable hydrogen production from nitrogen heterocycles, *Nat. Catal.*, 2022, **5**, 485–493.
6 D. Saha, H.-J. Yu, J. Wang, Prateek, X. Chen, C. Tang, C. Senger, J. N. Pagaduan, R. Katsumata, K. R. Carter, G. Zhou, P. Bai, N. Wu and J. J. Watkins, Mesoporous Single Atom-Cluster Fe–N/C Oxygen Evolution Electrocatalysts Synthesized with Bottlebrush Block Copolymer-Templated Rapid Thermal Annealing, *ACS Appl. Mater. Interfaces*, 2024, **16**, 13729–13744.
7 X. Lin, L. Zeng and M. Wu, Integrating single atoms with nanoparticle catalysts for efficient electrochemical energy conversion, *J. Mater. Chem. A*, 2024, **12**, 17793–17816.
8 W. Zheng and L. Y. S. Lee, Metal–Organic Frameworks for Electrocatalysis: Catalyst or Precatalyst?, *ACS Energy Lett.*, 2021, **6**, 2838–2843.
9 Y. Xiong, Y. Yang, F. J. DiSalvo and H. D. Abruña, Synergistic Bimetallic Metallic Organic Framework-Derived Pt–Co Oxygen Reduction Electrocatalysts, *ACS Nano*, 2020, **14**, 13069–13080.
10 H. B. Wu and X. W. Lou, Metal–organic frameworks and their derived materials for electrochemical energy storage and conversion: Promises and challenges, *Sci. Adv.*, 2017, **3**, eaap9252.
11 J. Zhao, J. Wang, Y. Tian, Y. Wang, E. Luo, J. Zhang, H. Xiao, M. Zhao, L. Zhang, T. Hu and J. Jia, Impact of heat treatment temperature of novel catalyst MnO_x@$Sm_2O_2CO_3$ for promoting oxygen reduction reaction, *Int. J. Hydrogen Energy*, 2024, **51**, 169–179.
12 A. O. Godoy, J. Foster, M. Dicome, G. McCool, B. Zulevi, M. Ostraat, S. Pylypenko and J. Jankovic, Understanding the Effects of Heat Treatment Temperature and

Atmosphere on Platinum Nanoparticle Sintering Processes on Different Engineered Catalyst Supports (ECS) for Fuel Cell Applications, *ACS Appl. Energy Mater.*, 2024, **7**, 951–964.

13 X. Lu and C. Zhao, Electrodeposition of hierarchically structured three-dimensional nickel–iron electrodes for efficient oxygen evolution at high current densities, *Nat. Commun.*, 2015, **6**, 6616.

14 L. Magnier, G. Cossard, V. Martin, C. Pascal, V. Roche, E. Sibert, I. Shchedrina, R. Bousquet, V. Parry and M. Chatenet, Fe–Ni-based alloys as highly active and low-cost oxygen evolution reaction catalyst in alkaline media, *Nat. Mater.*, 2024, **23**, 252–261.

15 D. Saha, C. L. Witt, R. Fatima, T. Uchiyama, V. Pande, D.-P. Song, H.-F. Fei, B. M. Yavitt and J. J. Watkins, Opportunities in Bottlebrush Block Copolymers for Advanced Materials, *ACS Nano*, 2025, **19**, 1884–1910.

16 H.-F. Fei, Y. Long, H.-J. Yu, B. M. Yavitt, W. Fan, A. Ribbe and J. J. Watkins, Bimodal Mesoporous Carbon Spheres with Small and Ultra-Large Pores Fabricated Using Amphiphilic Brush Block Copolymer Micelle Templates, *ACS Appl. Mater. Interfaces*, 2020, **12**, 57322–57329.

17 H.-F. Fei, W. Li, A. Bhardwaj, S. Nuguri, A. Ribbe and J. J. Watkins, Ordered Nanoporous Carbons with Broadly Tunable Pore Size Using Bottlebrush Block Copolymer Templates, *J. Am. Chem. Soc.*, 2019, **141**, 17006–17014.

18 H.-F. Fei, W. Li, S. Nuguri, H.-J. Yu, B. M. Yavitt, W. Fan and J. J. Watkins, One-Step Synthesis of Hierarchical, Bimodal Nanoporous Carbons *via* Co-templating with Bottlebrush and Linear Block Copolymers, *Chem. Mater.*, 2020, **32**, 6055–6061.

19 M. J. Jackman, K. L. Syres, D. J. H. Cant, S. J. O. Hardman and A. G. Thomas, Adsorption of Dopamine on Rutile TiO_2 (110): A Photoemission and Near-Edge X-ray Absorption Fine Structure Study, *Langmuir*, 2014, **30**, 8761–8769.

20 Q. Li, A. Bai, T. Zhang, S. Li and H. Sun, *Dopamine-derived nitrogen-doped carboxyl multiwalled carbon nanotube-modified graphite felt with improved electrochemical activity for vanadium redox flow batteries*, Royal Society*Open S*cience, 2020, vol. 7, p. 200402.

21 D. Saha, A. Bhardwaj, J. Wang, V. Pande, R. Hengstebeck, P. Bai and J. J. Watkins, Probing Electrocatalytic Synergy in Graphene/MoS2/Nickel Networks for Water Splitting through a Combined Experimental and Theoretical Lens, *ACS Appl. Mater. Interfaces*, 2024, **16**, 42254–42269.

22 D.-P. Song, A. Naik, S. Li, A. Ribbe and J. J. Watkins, Rapid, Large-Area Synthesis of Hierarchical Nanoporous Silica Hybrid Films on Flexible Substrates, *J. Am. Chem. Soc.*, 2016, **138**, 13473–13476.

23 D.-P. Song, W. Li, J. Park, H.-F. Fei, A. R. Naik, S. Li, Y. Zhou, Y. Gai and J. J. Watkins, Millisecond photothermal carbonization for *in situ* fabrication of mesoporous graphitic carbon nanocomposite electrode films, *Carbon*, 2021, **174**, 439–444.

24 U. Okoroanyanwu, A. Bhardwaj and J. J. Watkins, Large Area Millisecond Preparation of High-Quality, Few-Layer Graphene Films on Arbitrary Substrates *via* Xenon Flash Lamp Photothermal Pyrolysis and Their Application for High-Performance Micro-supercapacitors, *ACS Appl. Mater. Interfaces*, 2023, **15**, 13495–13507.

25 A. Bhardwaj, U. Okoroanyanwu, J. N. Pagaduan, W. Fan and J. J. Watkins, Large-Area Fabrication of Porous Graphene Networks on Carbon Fabric *via* Millisecond Photothermal Processing of Polyaniline for Supercapacitors, *Small*, 2024, **20**, 2402049.

26 V. A. P. Rodríguez, C. Rojas-Ayala, J. M. Medina, P. P. Cabrera, J. Quispe-Marcatoma, C. V. Landauro, J. R. Tapia, E. M. Baggio-Saitovitch and E. C. Passamani, $Fe_{50}Ni_{50}$ synthesized by high energy ball milling: a systematic study using X-ray diffraction, EXAFS and Mössbauer methods, *Mater. Charact.*, 2019, **149**, 249–254.

27 P. A. O'Day, J. J. Rehr, S. I. Zabinsky and G. E. Brown Jr., Extended X-ray Absorption Fine Structure (EXAFS) Analysis of Disorder and Multiple-Scattering in Complex Crystalline Solids, *J. Am. Chem. Soc.*, 1994, **116**, 2938–2949.

28 J. Woo, J. S. Lim, T. Lim, D. S. Baek, J. H. Kim, J. H. Lee, H. Y. Jeong, C. H. Choi and S. H. Joo, Fe–N/C catalysts with tunable mesoporous structures and carbon layer numbers reveal the role of interlayer O_2 activation, *EES Catal.*, 2023, **1**, 62–73.

29 Y. Zhou, Q. Zhou, H. Liu, W. Xu, Z. Wang, S. Qiao, H. Ding, D. Chen, J. Zhu, Z. Qi, X. Wu, Q. He and L. Song, Asymmetric dinitrogen-coordinated nickel single-atomic sites for efficient CO_2 electroreduction, *Nat. Commun.*, 2023, **14**, 3776.

30 Q. Jia, N. Ramaswamy, H. Hafiz, U. Tylus, K. Strickland, G. Wu, B. Barbiellini, A. Bansil, E. F. Holby, P. Zelenay and S. Mukerjee, Experimental Observation of Redox-Induced Fe–N Switching Behavior as a Determinant Role for Oxygen Reduction Activity, *ACS Nano*, 2015, **9**, 12496–12505.

31 Q. Jia, N. Ramaswamy, U. Tylus, K. Strickland, J. Li, A. Serov, K. Artyushkova, P. Atanassov, J. Anibal, C. Gumeci, S. C. Barton, M.-T. Sougrati, F. Jaouen, B. Halevi and S. Mukerjee, Spectroscopic insights into the nature of active sites in iron–nitrogen–carbon electrocatalysts for oxygen reduction in acid, *Nano Energy*, 2016, **29**, 65–82.

32 W. Wan, Y. Zhao, S. Wei, C. A. Triana, J. Li, A. Arcifa, C. S. Allen, R. Cao and G. R. Patzke, Mechanistic insight into the active centers of single/dual-atom Ni/Fe-based oxygen electrocatalysts, *Nat. Commun.*, 2021, **12**, 5589.

33 Z. Li, Y. Chen, S. Ji, Y. Tang, W. Chen, A. Li, J. Zhao, Y. Xiong, Y. Wu, Y. Gong, T. Yao, W. Liu, L. Zheng, J. Dong, Y. Wang, Z. Zhuang, W. Xing, C.-T. He, C. Peng, W.-C. Cheong, Q. Li, M. Zhang, Z. Chen, N. Fu, X. Gao, W. Zhu, J. Wan, J. Zhang, L. Gu, S. Wei, P. Hu, J. Luo, J. Li, C. Chen, Q. Peng, X. Duan, Y. Huang, X.-M. Chen, D. Wang and Y. Li, Iridium single-atom catalyst on nitrogen-doped carbon for formic acid oxidation synthesized using a general host–guest strategy, *Nat. Chem.*, 2020, **12**, 764–772.

34 D. Saha and P. Kruse, Editors' Choice—Review—Conductive Forms of MoS_2 and Their Applications in Energy Storage and Conversion, *J. Electrochem. Soc.*, 2020, **167**, 126517.

35 K. Zhu, X. Zhu and W. Yang, Application of *In Situ* Techniques for the Characterization of NiFe-Based Oxygen

Evolution Reaction (OER) Electrocatalysts, *Angew. Chem., Int. Ed.*, 2019, **58**, 1252–1265.
36 N. Todoroki, A. Shinomiya and T. Wadayama, Nanostructures and Oxygen Evolution Overpotentials of Surface Catalyst Layers Synthesized on Various Austenitic Stainless Steel Electrodes, *Electrocatalysis*, 2022, **13**, 116–125.
37 R. Kostecki and F. McLarnon, Electrochemical and *In Situ* Raman Spectroscopic Characterization of Nickel Hydroxide Electrodes: I. Pure Nickel Hydroxide, *J. Electrochem. Soc.*, 1997, **144**, 485.
38 J. Desilvestro, D. A. Corrigan and M. J. Weaver, Characterization of Redox States of Nickel Hydroxide Film Electrodes by *In Situ* Surface Raman Spectroscopy, *J. Electrochem. Soc.*, 1988, **135**, 885.
39 J. H. Hibben, The Raman Spectra of Water, Aqueous Solutions and Ice, *J. Chem. Phys.*, 1937, **5**, 166–172.
40 W. Sung, K.-i. Inoue, S. Nihonyanagi and T. Tahara, Unified picture of vibrational relaxation of OH stretch at the air/water interface, *Nat. Commun.*, 2024, **15**, 1258.
41 R. Anshari, M. Tsuboi, H. Sato, K. Tashiro and Y. Ozaki, Raman and ATR-FTIR unmask crystallinity changes and carboxylate group and vinyl group accumulation in natural weathering polypropylene microplastics, *Sci. Rep.*, 2025, **15**, 2518.
42 J. Jacob and M. A. Khadar, Investigation of mixed spinel structure of nanostructured nickel ferrite, *J. Appl. Phys.*, 2010, 107.
43 J. Landon, E. Demeter, N. İnoğlu, C. Keturakis, I. E. Wachs, R. Vasić, A. I. Frenkel and J. R. Kitchin, Spectroscopic Characterization of Mixed Fe–Ni Oxide Electrocatalysts for the Oxygen Evolution Reaction in Alkaline Electrolytes, *ACS Catal.*, 2012, **2**, 1793–1801.
44 L. Trotochaud, S. L. Young, J. K. Ranney and S. W. Boettcher, Nickel–Iron Oxyhydroxide Oxygen-Evolution Electrocatalysts: The Role of Intentional and Incidental Iron Incorporation, *J. Am. Chem. Soc.*, 2014, **136**, 6744–6753.
45 S. Chen, Z. Kang, X. Zhang, J. Xie, H. Wang, W. Shao, X. Zheng, W. Yan, B. Pan and Y. Xie, Highly Active Fe Sites in Ultrathin Pyrrhotite Fe_7S_8 Nanosheets Realizing Efficient Electrocatalytic Oxygen Evolution, *ACS Cent. Sci.*, 2017, **3**, 1221–1227.
46 K. I. Pandya, R. W. Hoffman, J. McBreen and W. E. O'Grady, In Situ X-Ray Absorption Spectroscopic Studies of Nickel Oxide Electrodes, *J. Electrochem. Soc.*, 1990, **137**, 383.
47 D. Friebel, M. W. Louie, M. Bajdich, K. E. Sanwald, Y. Cai, A. M. Wise, M.-J. Cheng, D. Sokaras, T.-C. Weng, R. Alonso-Mori, R. C. Davis, J. R. Bargar, J. K. Nørskov, A. Nilsson and A. T. Bell, Identification of Highly Active Fe Sites in (Ni, Fe)OOH for Electrocatalytic Water Splitting, *J. Am. Chem. Soc.*, 2015, **137**, 1305–1313.
48 H. Yu, M. E. Sweers, L. Osmieri, J. H. Park, A. J. Kropf, D. Yang, L. Ma, X. Lyu, A. Serov, D. A. Cullen, P. Zelenay, D. J. Myers and R. P. Hermann, Synergy between Ni and Fe in NiFe aerogel oxygen evolution reaction catalyst: *in situ* 57Fe Mössbauer and X-ray absorption spectroscopy studies, *EES Catal.*, 2025, **3**, 1229–1245.
49 Y.-F. Li and A. Selloni, Mechanism and Activity of Water Oxidation on Selected Surfaces of Pure and Fe-Doped NiOx, *ACS Catal.*, 2014, **4**, 1148–1153.
50 Y. Ou, L. P. Twight, B. Samanta, L. Liu, S. Biswas, J. L. Fehrs, N. A. Sagui, J. Villalobos, J. Morales-Santelices, D. Antipin, M. Risch, M. C. Toroker and S. W. Boettcher, Cooperative Fe sites on transition metal (oxy)hydroxides drive high oxygen evolution activity in base, *Nat. Commun.*, 2023, **14**, 7688.
51 Z. Wang, W. A. Goddard and H. Xiao, Potential-dependent transition of reaction mechanisms for oxygen evolution on layered double hydroxides, *Nat. Commun.*, 2023, **14**, 4228.
52 H. Xiao, H. Shin and W. A. Goddard, Synergy between Fe and Ni in the optimal performance of (Ni, Fe)OOH catalysts for the oxygen evolution reaction, *Proc. Natl. Acad. Sci. U. S. A.*, 2018, **115**, 5872–5877.
53 M. W. Louie and A. T. Bell, An Investigation of Thin-Film Ni–Fe Oxide Catalysts for the Electrochemical Evolution of Oxygen, *J. Am. Chem. Soc.*, 2013, **135**, 12329–12337.
54 L. Zhang, Y. Jia, G. Gao, X. Yan, N. Chen, J. Chen, M. T. Soo, B. Wood, D. Yang, A. Du and X. Yao, Graphene Defects Trap Atomic Ni Species for Hydrogen and Oxygen Evolution Reactions, *Chem*, 2018, **4**, 285–297.
55 H. A. Hansen, J. Rossmeisl and J. K. Nørskov, Surface Pourbaix diagrams and oxygen reduction activity of Pt, Ag and Ni(111) surfaces studied by DFT, *Phys. Chem. Chem. Phys.*, 2008, **10**, 3722–3730.
56 C.-H. Yeh and J.-J. Ho, Oxidation of CO on a carbon-based material composed of nickel hydroxide and hydroxyl graphene oxide, $(Ni_4(OH)_3$-hGO) – a first-principles calculation, *Phys. Chem. Chem. Phys.*, 2015, **17**, 7555–7563.
57 J. Cui, X. Liu, Y. Wei and X. Shen, A Synergistic effect on the atomic cluster M4 supported on MN4-graphene (M = Fe, Ni) for the hydrogen evolution reaction, *Phys. Chem. Chem. Phys.*, 2022, **24**, 11704–11712.
58 Y. Zhang, X. Chen, S. Gan, Y. Hu, Y. Tian, S. Wang, L. Chen, J. Xiao and N. Wang, Construction of highly active FeN_4@Fe_x(OH)y cluster composite sites for the oxygen reduction reaction and the oxygen evolution reaction, *Phys. Chem. Chem. Phys.*, 2023, **25**, 29173–29181.
59 F. T. de Oliveira, A. Chanda, D. Banerjee, X. Shan, S. Mondal, L. Que, E. L. Bominaar, E. Münck and T. J. Collins, Chemical and Spectroscopic Evidence for an Fe^V-Oxo Complex, *Science*, 2007, **315**, 835–838.
60 W. C. Ellis, N. D. McDaniel, S. Bernhard and T. J. Collins, Fast Water Oxidation Using Iron, *J. Am. Chem. Soc.*, 2010, **132**, 10990–10991.
61 M. Z. Ertem, L. Gagliardi and C. J. Cramer, Quantum chemical characterization of the mechanism of an iron-based water oxidation catalyst, *Chem. Sci.*, 2012, **3**, 1293–1299.
62 J. M. P. Martirez and E. A. Carter, Unraveling Oxygen Evolution on Iron-Doped β-Nickel Oxyhydroxide: The Key Role of Highly Active Molecular-like Sites, *J. Am. Chem. Soc.*, 2019, **141**, 693–705.

63 Z.-D. He, R. Tesch, M. J. Eslamibidgoli, M. H. Eikerling and P. M. Kowalski, Low-spin state of Fe in Fe-doped NiOOH electrocatalysts, *Nat. Commun.*, 2023, **14**, 3498.

64 A. Govind Rajan, J. M. P. Martirez and E. A. Carter, Strongly facet-dependent activity of iron-doped β-nickel oxyhydroxide for the oxygen evolution reaction, *Phys. Chem. Chem. Phys.*, 2024, **26**, 14721–14733.

65 J. M. P. Martirez and E. A. Carter, Effects of the Aqueous Environment on the Stability and Chemistry of β-NiOOH Surfaces, *Chem. Mater.*, 2018, **30**, 5205–5219.

66 M. Cococcioni and S. de Gironcoli, Linear response approach to the calculation of the effective interaction parameters in the $\mathrm{LDA}+\mathrm{U}$ method, *Phys. Rev. B*, 2005, **71**, 035105.

67 A. Govind Rajan, J. M. P. Martirez and E. A. Carter, Facet-Independent Oxygen Evolution Activity of Pure β-NiOOH: Different Chemistries Leading to Similar Overpotentials, *J. Am. Chem. Soc.*, 2020, **142**, 3600–3612.

68 M. J. Jang, S. H. Yang, M. G. Park, J. Jeong, M. S. Cha, S.-H. Shin, K. H. Lee, Z. Bai, Z. Chen, J. Y. Lee and S. M. Choi, Efficient and Durable Anion Exchange Membrane Water Electrolysis for a Commercially Available Electrolyzer Stack using Alkaline Electrolyte, *ACS Energy Lett.*, 2022, **7**, 2576–2583.

69 H. Koshikawa, H. Murase, T. Hayashi, K. Nakajima, H. Mashiko, S. Shiraishi and Y. Tsuji, Single Nanometer-Sized NiFe-Layered Double Hydroxides as Anode Catalyst in Anion Exchange Membrane Water Electrolysis Cell with Energy Conversion Efficiency of 74.7% at 1.0 A cm^{-2}, *ACS Catal.*, 2020, **10**, 1886–1893.

70 P. Ganesan, A. Sivanantham and S. Shanmugam, Inexpensive electrochemical synthesis of nickel iron sulphides on nickel foam: super active and ultra-durable electrocatalysts for alkaline electrolyte membrane water electrolysis, *J. Mater. Chem. A*, 2016, **4**, 16394–16402.

71 S. Li, T. Liu, W. Zhang, M. Wang, H. Zhang, C. Qin, L. Zhang, Y. Chen, S. Jiang, D. Liu, X. Liu, H. Wang, Q. Luo, T. Ding and T. Yao, Highly efficient anion exchange membrane water electrolyzers *via* chromium-doped amorphous electrocatalysts, *Nat. Commun.*, 2024, **15**, 3416.

72 A. Abdelhafiz, M. H. Mohammed, J. Abed, D.-C. Lee, M. Chen, A. S. Helal, Z. Ren, F. Alamgir, E. Sargent, P. A. Kohl, S. K. Elsaidi and J. Li, Tri-Metallic Catalyst for Oxygen Evolution Reaction Enables Continuous Operation of Anion Exchange Membrane Electrolyzer at 1A cm^{-2} for Hundreds of Hours, *Adv. Energy Mater.*, 2024, **14**, 2303350.